Acta Pharmaceutica Sinica B 2022;12(9):3650–3666

Chinese Pharmaceutical Association
Institute of Materia Medica, Chinese Academy of Medical Sciences

Acta Pharmaceutica Sinica B

www.elsevier.com/locate/apsb
www.sciencedirect.com

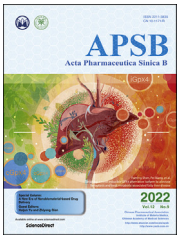

ORIGINAL ARTICLE

Targeting a novel inducible GPX4 alternative isoform to alleviate ferroptosis and treat metabolic-associated fatty liver disease

Jie Tong[a,†], Dongjie Li[a,h,†], Hongbo Meng[c,†], Diyang Sun[b], Xiuting Lan[a], Min Ni[a], Jiawei Ma[a], Feiyan Zeng[a,d], Sijia Sun[a], Jiangtao Fu[b], Guoqiang Li[b,e], Qingxin Ji[a], Guoyan Zhang[a], Qirui Shen[f], Yuanyuan Wang[a], Jiahui Zhu[a], Yi Zhao[a], Xujie Wang[a], Yi Liu[a], Shenxi Ouyang[a], Chunquan Sheng[g], Fuming Shen[a,*], Pei Wang[b,*]

[a]*Department of Pharmacy, Shanghai Tenth People's Hospital, Tongji University School of Medicine, Shanghai 200072, China*
[b]*Department of Pharmacology, School of Pharmacy, Naval Medical University/Second Military Medical University, Shanghai 200433, China*
[c]*Department of General Surgery, Shanghai Tenth People's Hospital, Tongji University School of Medicine, Shanghai 200072, China*
[d]*Department of Pharmacy, Shanghai Fourth People's Hospital, Tongji University School of Medicine, Shanghai 200081, China*
[e]*Shanghai Key Laboratory of Regulatory Biology, Institute of Biomedical Sciences and School of Life Sciences, East China Normal University, Shanghai 200241, China*
[f]*Chemical Biology Research Center, School of Pharmaceutical Sciences, Wenzhou Medical University, Wenzhou 325000, China*
[g]*Department of Medicinal Chemistry, School of Pharmacy, Naval Medical University/Second Military Medical University, Shanghai 200433, China*
[h]*Institute of Nuclear Medicine, Tongji University School of Medicine, Shanghai 200072, China*

Received 27 October 2021; received in revised form 22 December 2021; accepted 14 January 2022

*Corresponding authors.
E-mail addresses: pwang@smmu.edu.cn (Pei Wang), fumingshen@tongji.edu.cn (Fuming Shen).
[†]These authors made equal contributions to this work.
Peer review under responsibility of Chinese Pharmaceutical Association and Institute of Materia Medica, Chinese Academy of Medical Sciences.

https://doi.org/10.1016/j.apsb.2022.02.003

KEY WORDS

Ferroptosis;
GPX4;
Alternative isoform;
Fatty liver;
Oligomerization;
Methionine/choline-deficient diet;
High fat-fructose/sucrose diet;
Protein interaction

Abstract Metabolic-associated fatty liver disease (MAFLD), which is previously known as non-alcoholic fatty liver disease (NAFLD), represents a major health concern worldwide with limited therapy. Here, we provide evidence that ferroptosis, a novel form of regulated cell death characterized by iron-driven lipid peroxidation, was comprehensively activated in liver tissues from MAFLD patients. The canonical-GPX4 (cGPX4), which is the most important negative controller of ferroptosis, is downregulated at protein but not mRNA level. Interestingly, a non-canonical GPX4 transcript-variant is induced (inducible-GPX4, iGPX4) in MAFLD condition. The high fat-fructose/sucrose diet (HFFD) and methionine/choline-deficient diet (MCD)-induced MAFLD pathologies, including hepatocellular ballooning, steatohepatitis and fibrosis, were attenuated and aggravated, respectively, in cGPX4-and iGPX4-knockin mice. cGPX4 and iGPX4 isoforms also displayed opposing effects on oxidative stress and ferroptosis in hepatocytes. Knockdown of iGPX4 by siRNA alleviated lipid stress, ferroptosis and cell injury. Mechanistically, the triggered iGPX4 interacts with cGPX4 to facilitate the transformation of cGPX4 from enzymatic-active monomer to enzymatic-inactive oligomers upon lipid stress, and thus promotes ferroptosis. Co-immunoprecipitation and nano LC−MS/MS analyses confirmed the interaction between iGPX4 and cGPX4. Our results reveal a detrimental role of non-canonical GPX4 isoform in ferroptosis, and indicate selectively targeting iGPX4 may be a promising therapeutic strategy for MAFLD.

1. Introduction

Metabolic associated fatty liver disease (MAFLD), a new nomenclature emerged in 2020 for fatty liver replacing nonalcoholic fatty liver disease (NAFLD), remains as one leading cause for end-stage liver diseases[1]. Hepatic abnormalities in MAFLD encompass a wide array of clinicopathological spectrum of liver histology ranging from isolated hepatic steatosis to steatohepatitis and steatofibrosis, ultimately resulting in cirrhosis, liver failure and hepatocelluar carcinoma[2]. Unfortunately, the current understanding and therapy of MAFLD is still limited[3]. Ferroptosis is a novel form of regulated cell death (RCD) characterized by accumulation of iron-driven peroxidation of polyunsaturated fatty acids (PUFA), resulting in uncontrollable redox reaction, and ultimately, cell death[4−6]. As a unique type of RCD, ferroptosis is morphologically, biochemically, and genetically distinct from other well-known cell death categories including necrosis, apoptosis, autosis, and pyroptosis[7]. Although the precise signaling transduction has not been fully elucidated, ferroptosis has been shown to be regulated by glutathione peroxidase 4 (GPX4)[5,6,8,9], acyl-CoA synthetase long-chain family member 4 (ACSL4)[10], phosphatidylethanolamine binding protein 1[11], arachidonate 12/15-lipoxygenase (ALOX12/15)[12], ferroptosis suppressor protein 1 (FSP1)[13,14], poly-rC binding protein 1 (PCBP1)[15], transferrin receptor (TFR1)[16], ZIP14[17] and dihydroorotate dehydrogenase[18].

GPX4 has been established as the most important guardian against ferroptosis[5,6,8]. However, the concrete role of GPX4 in ferroptosis-associated pathophysiology is not fully clarified. Currently, four transcript variants of GPX4 in human and three GPX4 transcript variants in rodents are identified. Among these transcripts, the predominant variant 1 encodes the canonical GPX4 (cGPX4, GPX4 isoform A, ∼19 kDa), which is the first discovered defense factor to avoid lipid peroxidation[5,6,8]. Inactivation of cGPX4 is widely recognized as the primary cause of ferroptosis[5]. The human GPX4 isoform C was previously found to be mainly localized in testis and called sperm nuclei-GPX4 (nGPX4)[19], containing an alternate 5′ terminal exon, which results in an alternative isoform of GPX4 (∼34 kDa) with a distinct N-terminus. The complexity in *GPX4* gene transcription suggests the possible diverse functional roles of GPX4 under different pathophysiological conditions. However, most current studies regarding ferroptosis deemed the GPX4 isoform A (cGPX4) encoded by variant 1 as a negative biomarker for ferroptosis, ignoring the existence of other isoforms and their roles in ferroptosis.

In liver, ferroptosis is involved in high-iron diet-induced hemochromatosis[20] and contributes to the anticancer activity of sorafenib[21] and resistance to sorafenib[22] in hepatocellular carcinoma (HCC). Moreover, ferroptosis contributes to chemotherapy in nanoparticles-based tumor therapy[23−25]. Ferroptosis in hepatic stellate cells also participates in liver fibrosis[26,27]. As the hepatic iron deposition was more prevalent in patients with MAFLD-related HCC compared with HCC-free control patients[28], iron overload is deemed an independent risk factor for MAFLD. Several seminal studies recently depicted that iron chelators may prevent metabolic syndrome and steatohepatitis in experimental fatty liver models[29,30]. For example, knockout of the iron chaperone protein PCBP1 was shown to disrupt liver iron homeostasis, resulting in steatosis and inflammation in mice[15]. However, whether a cause-effect connection exists between MAFLD progression and ferroptosis remains largely unknown.

In the present study, we reported the existence of ferroptosis in liver tissues from MAFLD patients and two experimental MAFLD models. Intriguingly, although the canonical GPX4 isoform (cGPX4) was downregulated, the corresponding mRNA level remained unchanged in liver tissues from MAFLD patients. Conversely, a robust induction of nGPX4 was noted in liver tissues from MAFLD patients and mice. Our results demonstrated that this isoform was not limited in nuclei, and thus termed this inducible GPX4 transcript as ‘iGPX4’ herein. Steatohepatitis and liver injury were relieved in cGPX4-knockin mice but substantially aggravated in iGPX4-knockin mice in the face of MAFLD. Mechanistically, we found that upon lipid stress, the iGPX4 isoform directly interacted with cGPX4 and was incorporated into

the enzymatic-inactive high-molecular-weight GPX4 oligomers, ultimately lowering the enzymatic-active GPX4 monomer level. Our findings have illustrated a previously-unknown role of GPX4 alternative isoforms switch in ferroptosis regulation in MAFLD progression and should shed a light on the prevention and treatment of MAFLD.

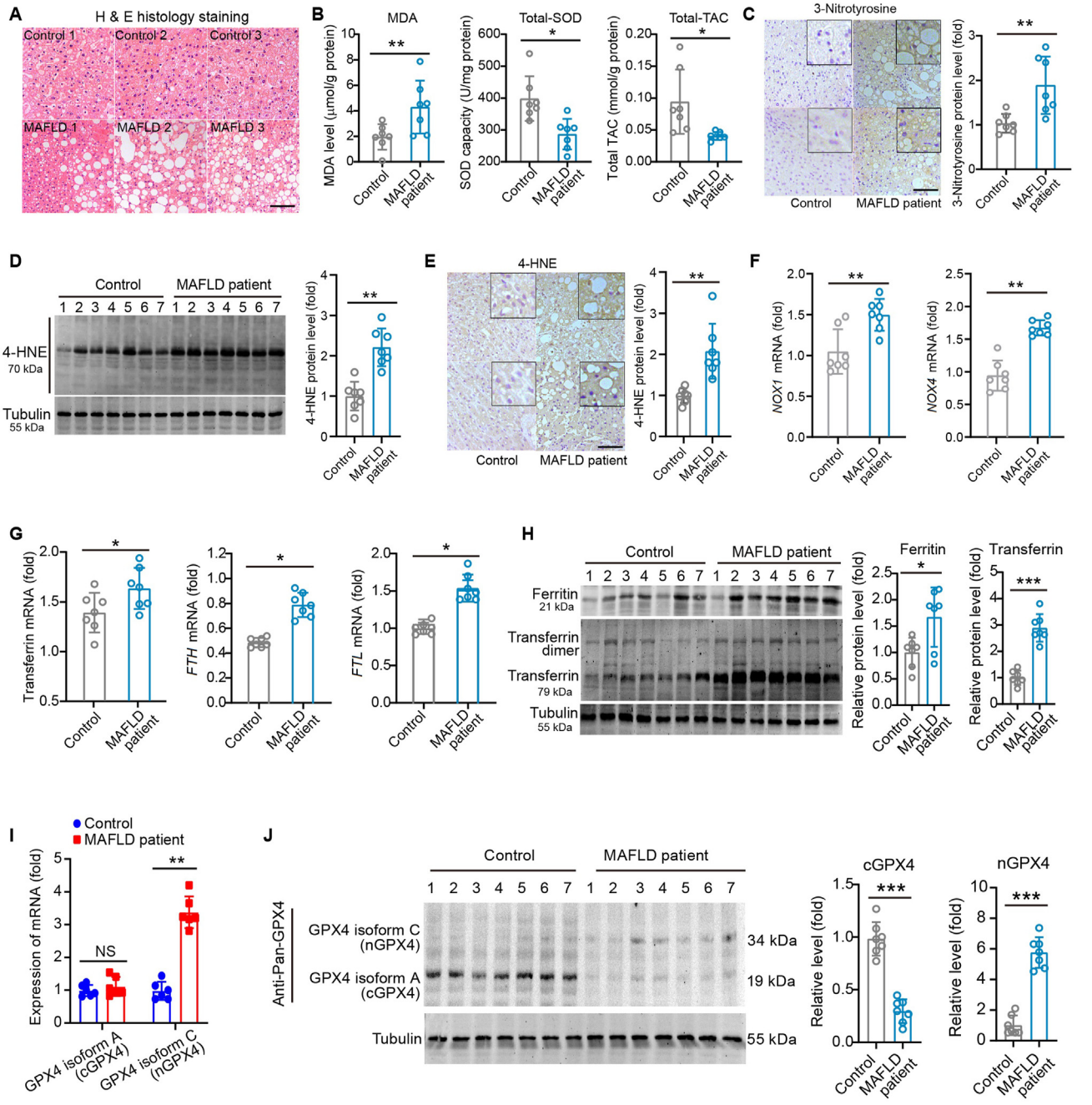

Figure 1 Ferroptosis is triggered in liver tissue of MAFLD patients. (A) Representative H&E histological analysis showing the MAFLD pathology in liver tissue from individuals with or without MAFLD ($n > 4$ images per individual). Scale bar, 100 μm. (B) The levels of MDA, total-SOD and total-TAC in liver from individuals with or without MAFLD. (C) Immunohistochemistry analysis of 3-nitrotyrosine in liver from individuals with or without MAFLD. Scale bar, 100 μm. (D, E) Immunoblotting (D) and immunohistochemistry analysis (E) of 4-HNE-protein adducts in liver from individuals with or without MAFLD. Quantitative analyses were performed. Scale bar, 100 μm. (F) The mRNA level of *NOX1* and *NOX4* in liver from individuals with or without MAFLD. (G) The mRNA level of transferrin, *FTH* and *FTL* in liver from individuals with or without MAFLD. (H) Immunoblotting analysis of ferritin and transferrin in liver from individuals with or without MAFLD. Transferrin dimer was also detected by the antibody against transferrin in immunoblotting. Tubulin was used as a loading control in immunoblotting. (I) Relative mRNA levels of *GPX4* isoform A and C in liver tissue from human with or without MAFLD. (J) Detection of GPX4 isoform A and GPX4 isoform C in liver tissues from human with or without MAFLD. Data are presented as mean ± SEM and analyzed by unpaired *t*-test, $n = 7$ per group; $^{*}P < 0.05$, $^{**}P < 0.01$, $^{***}P < 0.001$ *vs.* Control.

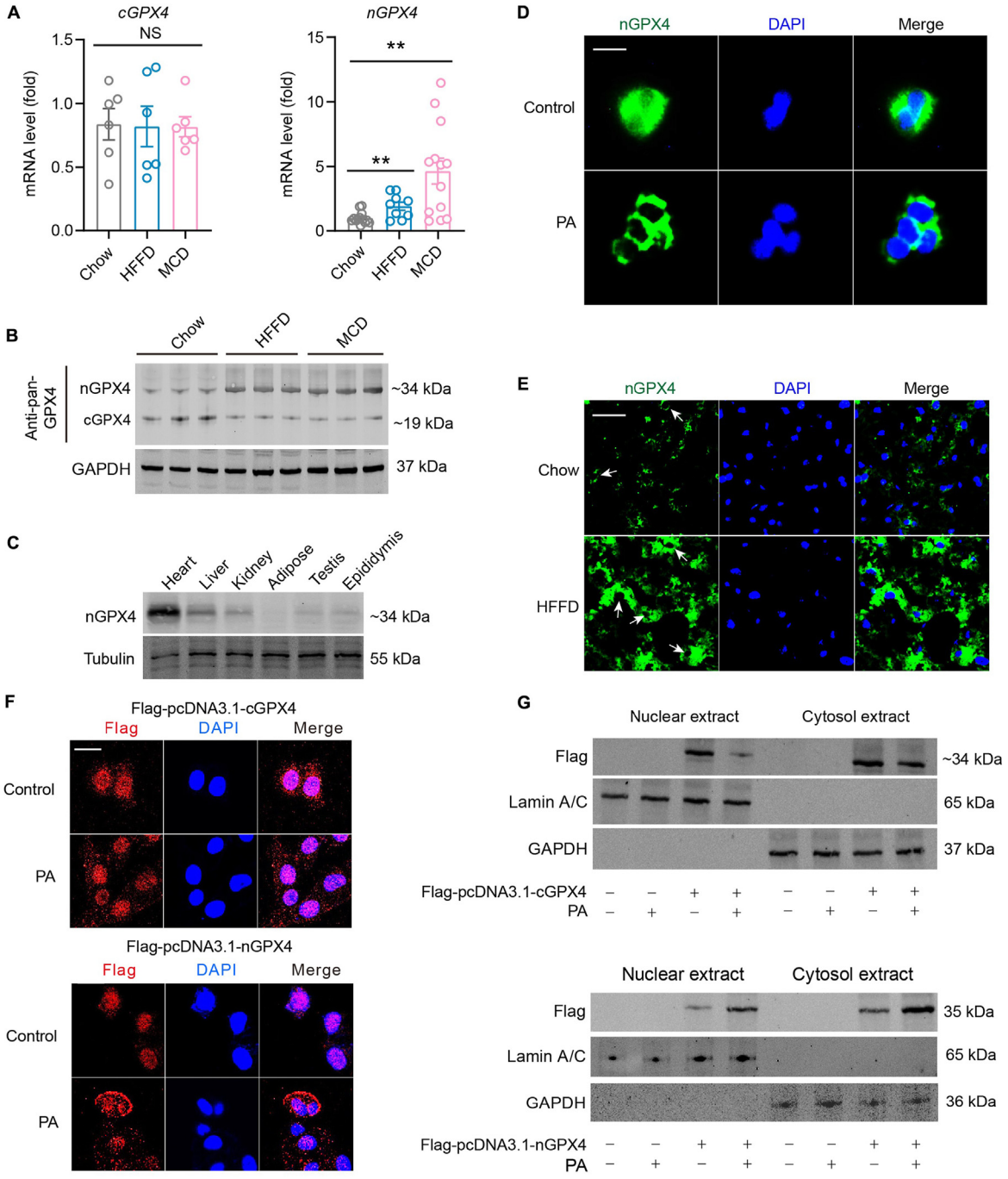

Figure 2 Identification of a novel inducible GPX4 alternative isoform triggered upon lipid peroxidation stress. (A) The change mRNA levels of *cGPX4* and *nGPX4* in liver tissues from MAFLD mice induced by HFFD and MCD ($n = 6$ per group). (B) The change protein levels of cGPX4 and nGPX4 in liver tissues from MAFLD mice induced by HFFD and MCD ($n = 3$ per group). (C) Protein expression of nGPX4 in various mouse tissues was determined by immunoblotting with a polyclonal antibody against a specific amino acid sequence (SPRKRPGPRRRKARC) within the N-terminal of mouse nGPX4. (D) The distribution of nGPX4 in AML12 hepatocytes was determined by immunofluorescence with a polyclonal antibody against mouse nGPX4. DAPI was used to stain nuclei ($n = 6$ per group). Scale bar, 20 μm. (E) The nGPX4 was determined by immunofluorescence with a polyclonal antibody against mouse nGPX4 in liver tissue from Chow- or HFFD-treated mice ($n = 6$ per group). DAPI was used to stain nuclei. Scale bar, 100 μm. (F) Flag-tagged cGPX4 and nGPX4 were transfected into AML12 hepatocytes, and the subcellular localization of cGPX4 and nGPX4 was detected with a mouse monoclonal antibody recognizing Flag followed by an Alexa Fluor 568 goat-anti-mouse secondary antibody ($n = 3$ per group). DAPI was used to stain nuclei (blue). Scale bar, 20 μm. (G) Flag-tagged cGPX4 and nGPX4 were transfected into AML12 hepatocytes, and the cytosol and nuclear fractions were extracted to assess subcellular localization of cGPX4 and nGPX4 by immunoblotting with a mouse monoclonal antibody recognizing Flag ($n = 3$ per group). Lamin A/C was used a loading control for nuclear extract while GAPDH was used a loading control for cytosol extract. Data are presented as mean ± SEM and analyzed by one-way ANOVA, followed by Tukey's HSD test; $^{**}P < 0.01$ *vs*. Chow. NS, no significance.

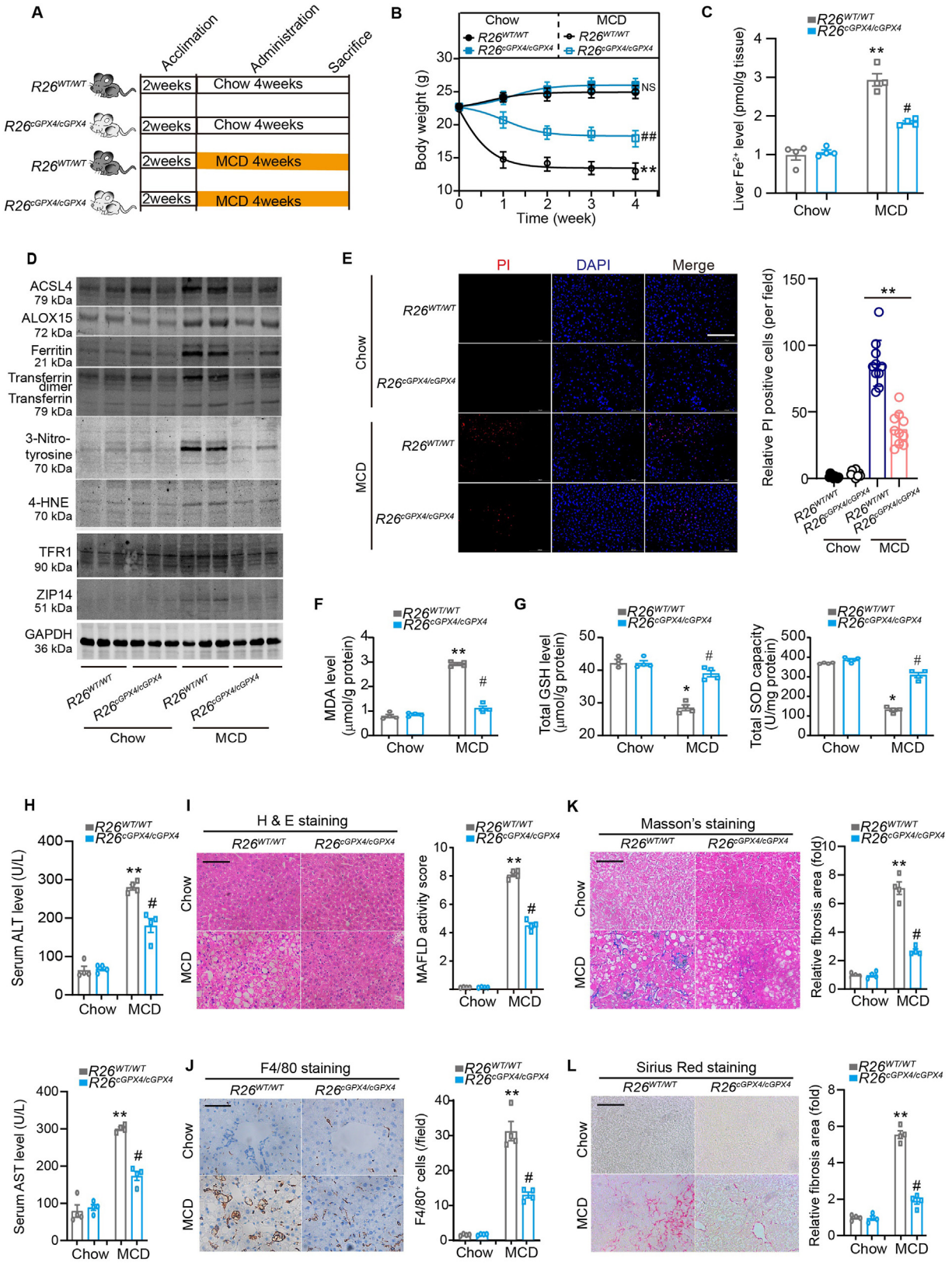

Figure 3 Knockin of cGPX4 inhibits ferroptosis and protects against MAFLD in mice. (A) Scheme illustrating experimental design for comparing MCD-induced MAFLD pathologies between $R26^{WT/WT}$ and $R26^{cGPX4/cGPX4}$ mice. (B) The body weight curves of $R26^{WT/WT}$ and $R26^{cGPX4/cGPX4}$ mice fed a MCD or a normal Chow diet ($n = 6$ per group). (C) The Fe^{2+} levels in liver tissues of $R26^{WT/WT}$ and $R26^{cGPX4/cGPX4}$ mice fed a MCD or a normal Chow diet ($n = 5$ per group). (D) Immunoblotting of ACSL4, ALOX15, ferritin, transferrin, 3-nitrotyrosine, 4-HNE, TFR1 and ZIP14 in liver tissues of $R26^{WT/WT}$ and $R26^{cGPX4/cGPX4}$ mice fed a MCD or a normal Chow diet ($n = 3$ per group). (E) PI staining

2. Materials and methods

2.1. Human liver samples

Human normal liver tissue samples ($n = 14$) were obtained from individuals (>18 years old) who underwent hepatectomy due to hepatolithiasis, liver trauma or hepatic haemangioma at Shanghai Tenth People's Hospital (Shanghai, China). With the preoperative ultrasound scanning and intraoperative observation/examination, patients with MAFLD at different stages including simple fatty liver, nonalcoholic steatohepatitis and liver fibrosis were included. The histological changes in these samples were confirmed by H&E staining. The normal liver tissues in the same patient were collected for comparison. Individuals meeting any of the following criteria were excluded from this study: excessive alcohol consumption (>140 g for men or >70 g for women, per week), drug or toxin use, viral infection (*e.g.*, AIDS, hepatitis B virus and hepatitis C virus), coronary heart disease, myocardial infarction, or cerebral apoplexy. According to the histological analysis, liver tissues form 14 cases (7 control individuals and 7 MAFLD patients) were used, 8 from men and 6 from women. The study was approved by the institutional research ethics committee of Shanghai Tenth People's Hospital of Tongji University (approval number: SHSY-IEC-4.1/19-126/01) and conducted in accordance with the ethical standards of the Helsinki Declaration. Informed consent was obtained from each recruited patient. All of the participants included underwent physical, anthropometric, and biochemical assessments.

2.2. Mice

All experimental procedures in mice were reviewed and approved by Institutional Animal Care and Use Committee of Medical School of Tongji University and the Animal Care and Use Committee of Tongji University (Shanghai, China). The animals received humane care according to the criteria outlined in the Guide for the Care and Use of Laboratory Animals prepared by the National Academy of Sciences and published by the National Institutes of Health. All the mice were housed in a temperature-controlled environment (23 ± 2 °C) with free access to water and chow under a 12-h/12-h light/dark cycle. Every effort was made to minimize the use of the animals and their discomfort. Animal Health status including body weight measurement, behavior observation and responses to external stimuli, was checked daily.

2.3. Generation of knockin mice

The two gene knockin mouse stains harboring cGPX4 ($R26^{cGPX4/cGPX4}$, project No. KICMS181221LY4) and iGPX4 ($R26^{iGPX4/iGPX4}$, project No. KICMS170117PL1) respectively were generated by Cas9/CRISPR-mediated genome editing (Cyagen Biosciences, Santa Clara, CA, USA). For $R26^{cGPX4/cGPX4}$ and $R26^{iGPX4/iGPX4}$ mice generation, the "CAG-mouse cGPX4 cDNA (NM_008162.3)-polyA" cassette and "CAG-mouse iGPX4 cDNA (NM_001037741.3)-polyA" cassettes were inserted into intron 1 of *Rosa26* respectively under the guide of gDNA. The homology arms were generated by PCR using BAC clone as template. The pups were genotyped by PCR followed by sequencing analysis confirmation for positive targeting, which was further verified by Southern blot. See Supporting Information Fig. S3A−S3D ($R26^{cGPX4/cGPX4}$) and Fig. S4A−S4D ($R26^{iGPX4/iGPX4}$) for more detailed information on the two strains of knockin mice. These mice were backcrossed for at least six generations with C57BL/6J mice (Vital River Laboratories).

2.4. Generation of a polyclonal antibody against iGPX4 isoform

The polyclonal antibody specifically against iGPX4 isoform was developed by GeneScript (NJ, USA). Briefly, the lyophilized synthesized amino acids sequence SPRKRPGPRRRKARC (Lot.: C170GEG170-1) conjugated with KLH were injected into New Zealand Rabbit and the pre-immune serum was collected and then affinity-purified antibody was produced. The final concentration of the generated affinity-purified antibody against iGPX4 isoform is 0.118 mg/mL.

2.5. High fat-fructose/sucrose diet (HFFD)-induced MAFLD model

A mouse model of MAFLD was established by feeding the 8-week-old male mice with a HFFD diet (20% protein, 60% fat, and 20% carbohydrates; D12942; Research Diets, NJ, USA) for 16 weeks. The mice received a high fructose/sucrose solution (55% fructose and 45% sucrose) *ad libitum* to promote the development of MAFLD[31]. Mice were fed a normal chow diet (4% fat, 78% carbohydrate and 18% protein) and normal water served as control mice.

2.6. Methionine/choline-deficient diet (MCD)-induced MAFLD model

Another mouse model of MAFLD was established by feeding the 8-week-old male mice a MCD diet (A02082002B; Research Diets, NJ, USA) for 4 weeks. Mice were fed a normal chow diet and pure water served as controls.

2.7. Statistical analysis

All experimental values are presented as the mean ± standard error of mean (SEM). Results analysis was performed using GraphPad Prism 8.0 (La Jolla, CA, USA) using unpaired *t*-test or analysis of variance (ANOVA) followed by Tukey *post hoc* test.

showing the cell death in liver tissue of $R26^{WT/WT}$ and $R26^{cGPX4/cGPX4}$ mice fed MCD or normal chow ($n = 10$ per group). DAPI was used to label nuclei. Scale bars, 100 μm. (F, G) The levels of MDA (F), GSH and SOD (G) in liver tissues from $R26^{WT/WT}$ and $R26^{cGPX4/cGPX4}$ mice fed with Chow or MCD ($n = 3$ per group). (H) Serum ALT and AST levels in $R26^{WT/WT}$ and $R26^{cGPX4/cGPX4}$ mice fed a MCD or a normal Chow diet ($n = 4$ per group). (I) MAFLD activity score calculated based on H&E staining in liver from $R26^{WT/WT}$ and $R26^{cGPX4/cGPX4}$ mice fed a MCD or a normal Chow diet ($n = 4$ per group). Scale bars, 100 μm. (J) Immunohistochemistry staining of F4/80 in liver from $R26^{WT/WT}$ and $R26^{cGPX4/cGPX4}$ mice fed a MCD or a normal Chow diet ($n = 4$ per group). Scale bar, 100 μm. (K, L) Liver fibrosis was determined by Masson's trichrome staining (K) and Sirius Red staining (L). Quantitative analyses were performed ($n = 4$ per group). Scale bars, 100 μm. Data are presented as mean ± SEM. Data were analyzed by two-way ANOVA followed by Tukey's HSD test; $^{*}P < 0.05$, $^{**}P < 0.01$ *vs.* Chow; $^{\#}P < 0.05$, $^{\#\#}P < 0.01$ *vs.* $R26^{WT/WT}$ mice + MCD. NS, no significance.

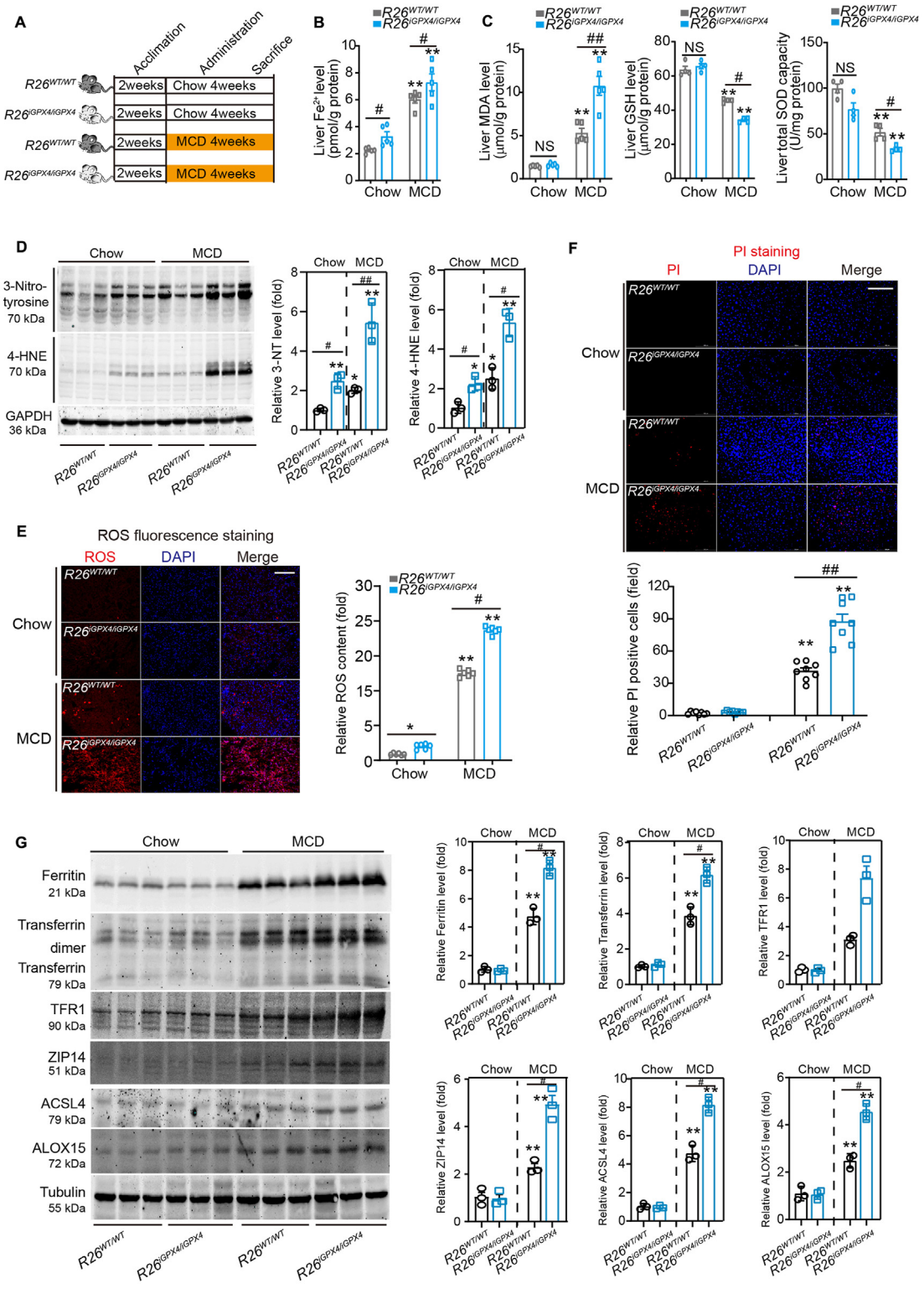

Figure 4 Knockin of iGPX4 promotes ferroptosis in MAFLD murine model. (A) Scheme illustrating experimental design for comparing MCD-induced MAFLD pathologies between $R26^{WT/WT}$ and $R26^{iGPX4/iGPX4}$ mice. (B) The Fe^{2+} level in liver tissues from $R26^{WT/WT}$ and $R26^{iGPX4/iGPX4}$ mice fed MCD or normal chow ($n = 5$ per group). (C) The levels of MDA, GSH and SOD in liver tissues from $R26^{WT/WT}$ and $R26^{iGPX4/iGPX4}$ mice fed MCD or normal chow ($n = 4-5$ per group). (D) Immunoblotting analyses of 3-nitrotyrosine and 4-HNE protein adducts in liver from $R26^{WT/WT}$ and $R26^{iGPX4/iGPX4}$ mice under Chow or MCD conditions ($n = 3$ per group). (E) ROS production in liver from $R26^{WT/WT}$ and $R26^{iGPX4/iGPX4}$ mice fed MCD or normal chow ($n = 6$ per group). Scale bar, 100 μm. (F) PI staining showing the cell death in liver tissue of $R26^{WT/WT}$ and $R26^{iGPX4/iGPX4}$ mice fed MCD or normal chow. DAPI was used to label nuclei ($n = 8$ per group). Scale bars, 100 μm. (G) Immunoblotting analyses of ferroptosis-associated proteins Ferritin, Transferrin, TFR1, ZIP14, ACSL4 and ALOX15 in liver from $R26^{WT/WT}$ and $R26^{iGPX4/iGPX4}$ mice fed MCD or normal chow. $n = 3$ per group. Data are presented as mean ± SEM and analyzed by two-way ANOVA followed by Tukey's *post hoc* test; $^{*}P < 0.05$, $^{**}P < 0.01$ *vs.* Chow; $^{\#}P < 0.05$, $^{\#\#}P < 0.01$ *vs.* $R26^{WT/WT}$ mice + MCD. NS, no significance.

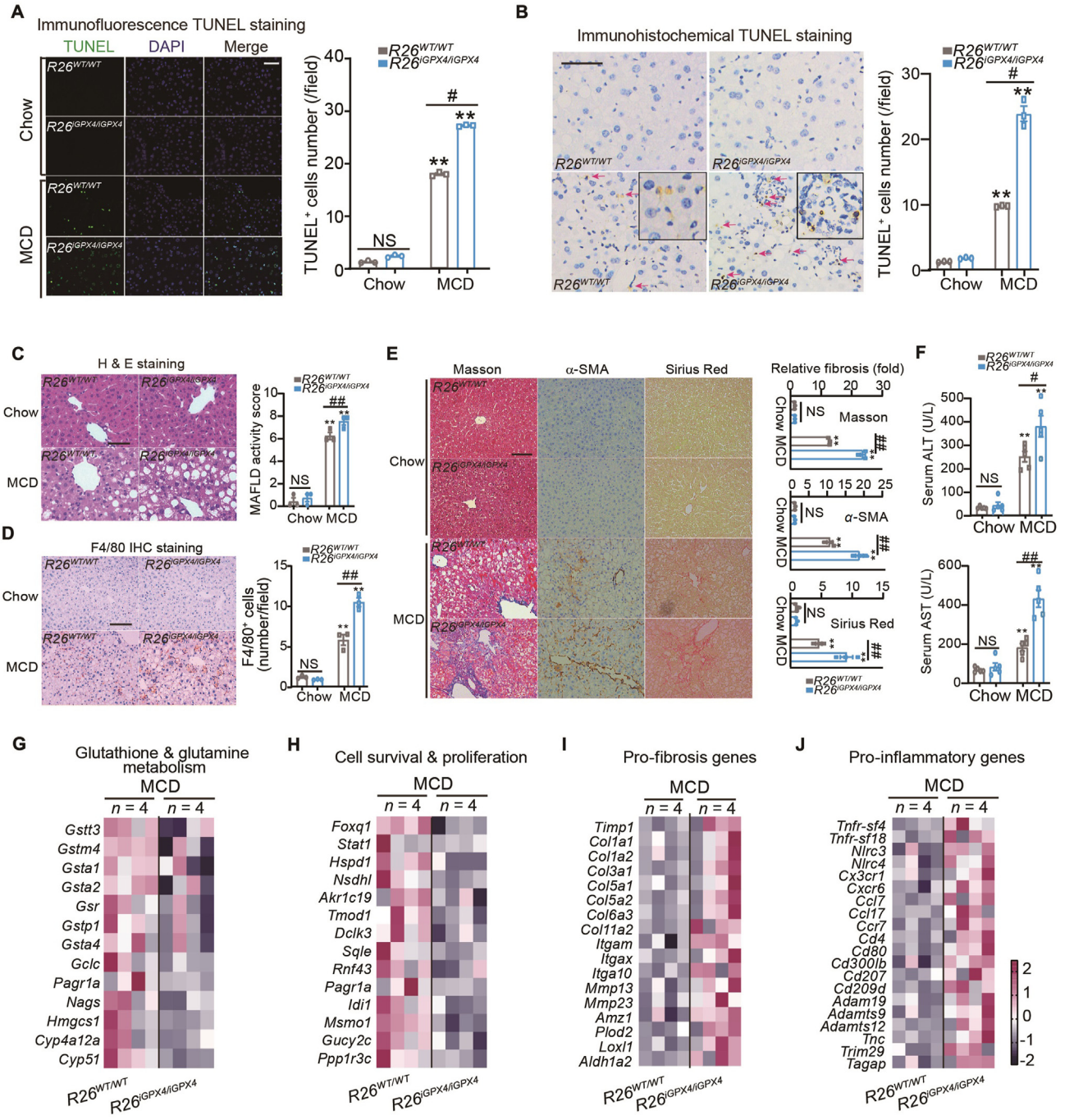

Figure 5 Knockin of iGPX4 exacerbates liver damage in MAFLD model. (A, B) Immunofluorescence (A) and immunohistochemistry (B) TUNEL assays in liver tissues from $R26^{WT/WT}$ and $R26^{iGPX4/iGPX4}$ mice under Chow or MCD conditions ($n = 3$ per group). Scale bars, 100 μm. (C) H&E staining and MAFLD activity score in liver tissues from $R26^{WT/WT}$ and $R26^{iGPX4/iGPX4}$ mice under Chow or MCD conditions ($n = 3$ per group). Scale bar, 100 μm. (D) Immunohistochemistry staining of F4/80 in liver tissues from $R26^{WT/WT}$ and $R26^{iGPX4/iGPX4}$ mice under Chow or MCD conditions ($n = 3$ per group). Scale bar, 100 μm. (E) Liver fibrosis was determined by Masson's trichrome staining, α-SMA immunohistochemistry staining and Sirius Red staining in liver tissues from $R26^{WT/WT}$ and $R26^{iGPX4/iGPX4}$ mice under Chow or MCD conditions ($n = 3$ per group). Scale bar, 100 μm. (F) Serum ALT and AST levels in $R26^{WT/WT}$ and $R26^{iGPX4/iGPX4}$ mice under Chow or MCD conditions ($n = 5$ per group). (G–J) Heatmap derived from RNA-sequencing assay indicating the altered genes (red, upregulated; blue, downregulated) involved in glutathione and glutamine metabolism, cell survival a prolifendration, fibrosis and inflammation between $R26^{iGPX4/iGPX4}$ mice and $R26^{WT/WT}$ mice liver tissues under MCD condition ($n = 4$ per group). Criteria: a fold change >1.5 and a corresponding adjusted P value < 0.05. Data are presented as mean ± SEM. Data was analyzed two-way ANOVA followed by Tukey's HSD test or unpaired t-test; $^{**}P < 0.01$ *vs.* Chow; $^{\#}P < 0.05$, $^{\#\#}P < 0.01$ *vs.* $R26^{WT/WT}$ mice + MCD. NS, no significance.

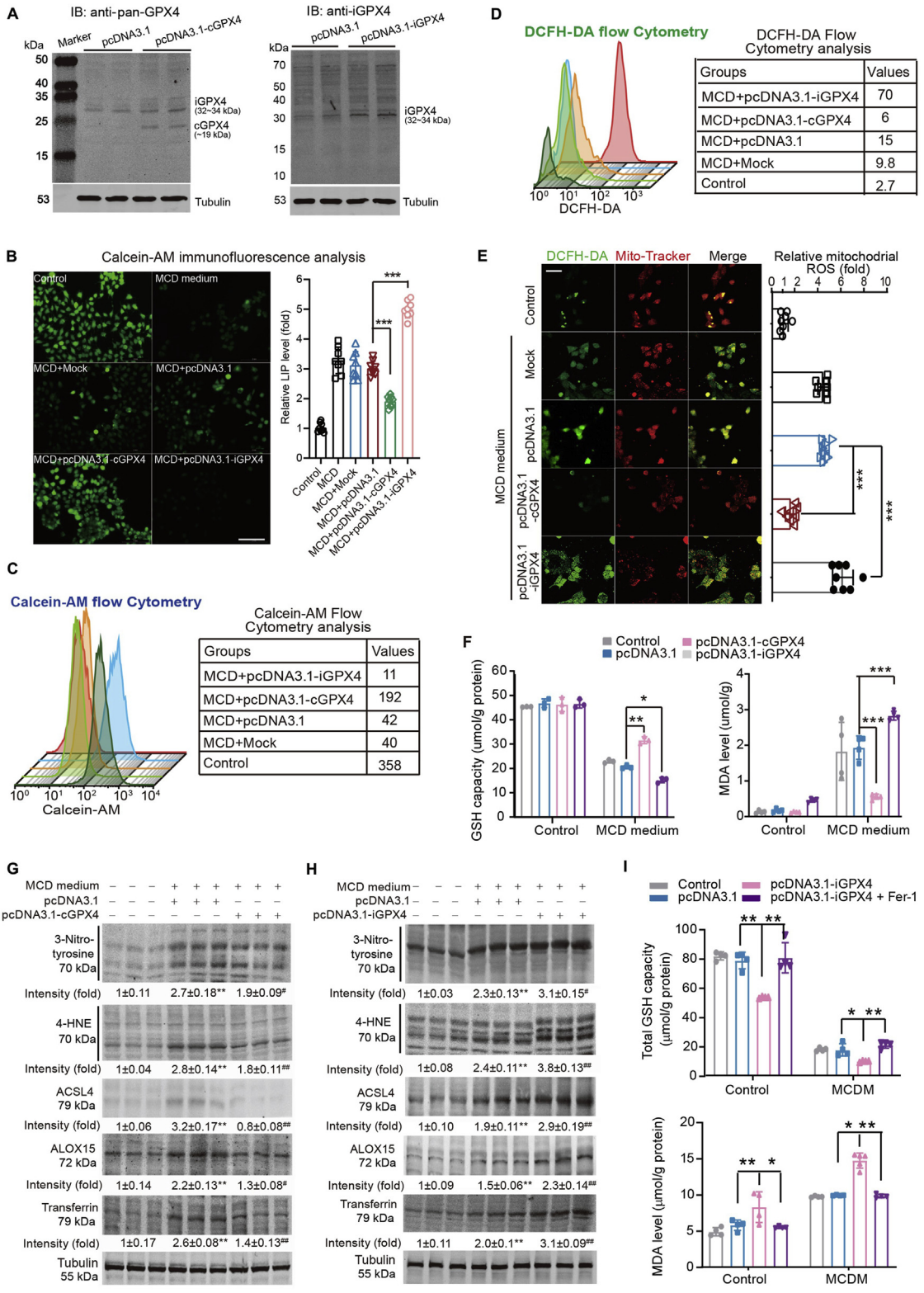

Figure 6 cGPX4 and iGPX4 isoforms have opposing effects on ROS production and ferroptosis in hepatocytes upon lipid stress. (A) Immunoblotting confirms the overexpression of cGPX4 and iGPX4 in AML12 hepatocytes transfected with pcDNA3.1-cGPX4 and pcDNA3.1-iGPX4 respectively. The anti-Pan-GPX4 antibody was used in left panel and the specific antibody against iGPX4 generated by us was used in right panel ($n = 3$ per group). (B, C) Fe^{2+} pool in AML12 hepatocytes was determined by immunofluorence analysis (B) and flow cytometry analysis (C). AML12 hepatocytes were transfected with pcDNA3.1-cGPX4 and pcDNA3.1-iGPX4 and then stimulated under methionine- and choline-deficient medium (MCDM). Calcein-AM probe was added into the medium (final concentration: 10 mol/L) for 30 min to monitorμ the Fe^{2+} pool under confocal microscopy or evaluated with flow cytometry ($n = 6-8$ per group). Scale bar, 100 μm. (D, E) ROS level in AML12

For nonparametric data such as MAFLD activity score, Mann−Whitney U test was performed. A P value < 0.05 was considered to be significant.

See other methods in Supporting Information.

3. Results

3.1. Ferroptosis is triggered in liver tissue of MAFLD patients

To decipher the involvement of ferroptosis in clinical MAFLD, normal liver tissues were collected from 14 individuals with ($n = 7$) or without MAFLD (control, $n = 7$). These patients underwent hepatectomy due to hepatolithiasis, liver trauma or hepatic haemangioma. The anthropometric information of these patients was shown in Supporting Information Fig. S1A. The morphological characterization of MAFLD was confirmed under visual inspection during the hepatectomy and histology analysis using H&E staining (Fig. 1A). The level of lipid peroxidation marker malondialdehyde (MDA) was elevated, whereas activity of total superoxide dismutase (SOD) and total antioxidant capacity (TAC) were decreased in liver tissues from MAFLD patients (Fig. 1B). Immunohistochemistry staining of 3-nitrotyrosine, a marker of peroxynitrite-mediated nitration, showed a much higher nitration of amino acid residues in liver tissue of MAFLD patients (Fig. 1C). Both immunoblotting and immunohistochemistry analyses in human MAFLD liver tissues demonstrated a significantly elevated level of 4-hydroxynonenal (4-HNE), produced following lipid peroxidation and formation of stable 4-HNE-protein adducts (Fig. 1D and E). The mRNA levels of NADPH oxidase 1 (*NOX1*) and *NOX4* were also higher in livers from MAFLD patients (Fig. 1F). These denoted evident lipid peroxidation in liver tissues of MAFLD patients.

To better define the ferroptosis-related iron profile, we quantified levels of several iron-associated factors. The mRNA levels of transferrin, ferritin heavy chain (*FTH*) and ferritin light chain (*FTL*) were significantly higher in MAFLD patient livers compared with those from controls (Fig. 1G). At protein level, significant higher levels of ferritin and transferrin were detected using immunoblotting and immunohistochemistry respectively (Fig. 1H and Fig. S1B). Next, we measured mRNA levels of ferroptosis protector *GPX4*. Although there is no previous information on the four known *GPX4* transcript variants in liver, we examined them in human liver tissues using quantitative PCR (qPCR) analysis. We designed specific primers targeting variants 1, 2 and 3, which encodes isoform A, B and C, respectively (Supporting Information Fig. S2A) and determined their mRNA expression in human liver tissue. It was found that *GPX4* isoform A (cGPX4) and isoform C (nGPX4) had comparable mRNA levels, while isoform B was expressed at a level much lower (Fig. S2B). We chose to further investigate cGPX4 and nGPX4 in human liver tissue. Unexpectedly, cGPX4 mRNA levels did not differ in individuals with or without MAFLD (Fig. 1I). In contrast, the mRNA level of nGPX4 in MAFLD patient liver tissues was 3.5-fold higher than that in control subjects (Fig. 1I). Immunoblotting analysis using an anti-pan-GPX4 antibody showed that cGPX4 was downregulated while nGPX4 was upregulated in MAFLD patient liver tissues (Fig. 1J). These results indicate that ferroptosis is comprehensively triggered in liver tissue of MAFLD patients, and the modulation of GPX4 upon MAFLD condition seems far more complex than previously reported[29,30].

3.2. Identification of a novel inducible GPX4 alternative isoform triggered upon lipid peroxidation stress

To ascertain the change of GPX4 isoforms in liver under MAFLD condition, we evaluated levels of GPX4 isoforms in experimental MAFLD murine models evoked by either 16-week HFFD or 4-week MCD, two well-established animal models for MAFLD[32]. Similar to our observation in MAFLD patients, mRNA expression of cGPX4 was unaffected although that of nGPX4 was significantly induced in livers from HFFD- and MCD-fed mice (Fig. 2A), suggesting that the transcription of nGPX4 may be triggered in the face of MAFLD condition in both human and mice. Similar effects were observed in cultured AML12 hepatocytes (Fig. S2C). Immunoblotting with a pan-GPX4 antibody showed that nGPX4 was significantly upregulated, whereas cGPX4 was downregulated in the liver tissues of HFFD- or MCD-fed mice (Fig. 2B).

Since there is no commercial antibody can specifically discriminate the nGPX4 isoform from other isoforms, we generated a rabbit polyclonal antibody specifically against the amino acid sequence (SPRKRPGPRRRKARC) within N-terminal of mouse nGPX4. With this antibody, we found that the nGPX4 was expressed abundantly in mouse heart and moderately in liver and kidney using this antibody (Fig. 2C). By contrast, testis, epididymis and adipose did not express high levels of nGPX4 (Fig. 2C), which is different from previous report showing it was mainly expressed in sperms[19]. We next evaluated the distribution of nGPX4 in cultured hepatocytes and liver tissues using this antibody. Immunofluorescent staining in AML12 cells showed that the nGPX4 isoform was expressed in both nucleus and cytoplasm in normal condition, but was detected mainly in cytoplasm upon PA stress condition (Fig. 2D). In mice liver sections, most of iGPX4 was detected in cytoplasm in both normal and stress conditions (Fig. 2E). Moreover, it is notable that expression of iGPX4 in HFFD-fed mice liver was largely enhanced compared with that in chow-fed mice liver, suggesting an induction of iGPX4 (Fig. 2E). Further, we generated plasmids carrying Flag-tagged cGPX4 and nGPX4 and transfected into AML-12 mouse hepatocytes for examination of

hepatocytes was determined by flow cytometry analysis (D) and immunofluorence analysis (E). AML12 hepatocytes were transfected with pcDNA3.1-cGPX4 and pcDNA3.1-iGPX4 and then stimulated under MCDM. In flow cytometry analysis, DCFH-DA fluorescence was analyzed. In immunofluorence analysis, DCFH-DA (5 μmol/L) and Mitotracker-Red-CMXRos dyes (200 nmol/L) were added into the medium for 30 min ($n = 6$−8 per group). The DCFH-DA fluorescence (green) and mitochondrial fluorescence (red) were visualized under a FV1000 confocal microscopy. Scale bar, 100 μm. (F) The levels of GSH and MDA in AML12 hepatocytes transfected with pcDNA3.1-cGPX4 and pcDNA3.1-iGPX4 plasmids respectively under normal culture medium or MCDM ($n = 4$ per group). (G, H) Immunoblotting analyses of 3-nitrotyrosine, 4-HNE, ACSL4, ALOX15 and Transferrin in AML12 hepatocytes transfected with plasmid of pcDNA3.1-cGPX4 (G) or pcDNA3.1-iGPX4 (H) under normal culture medium or MCDM ($n = 3$ per group). (I) The levels of GSH activity and MDA in AML12 hepatocytes transfected with pcDNA3.1-iGPX4 plasmids with or without ferroptosis inhibitor Fer-1 (100 nmol/L) under normal culture medium or MCDM ($n = 4$ per group). Data are presented as mean ± SEM and analyzed by two-way ANOVA followed by Tukey's *post hoc* test; $^{*}P < 0.05$, $^{**}P < 0.01$, $^{***}P < 0.001$.

distribution of fusion protein using Flag-tag probe. Immunofluorescent staining showed that the forced-expressed nGPX4 protein was mainly localized in nucleus under normal condition but re-distributed into cytosols upon PA challenge (Fig. 2F). Immunoblotting analysis also showed that the forced-expressed cGPX4 was validated in both cytosol and nucleus, and was down-regulated upon palmitic acid (PA) stress, an *in vitro* MAFLD model (Fig. 2G). The forced-expressed nGPX4 was observed in nucleus under normal condition but was significantly induced in cytosol extracts upon PA (Fig. 2G). Considering the fact that the name nGPX4 may not reflect its feature and it was obviously triggered upon lipid stress, we termed this GPX4 isoform as "inducible-GPX4" (iGPX4).

3.3. *Isoform cGPX4 inhibits ferroptosis and protects against MAFLD in mice*

Individual mammalian genes often produce multiple protein isoforms with similar, distinct or even opposing biological actions through alternative splicing or transcription start-site switching[33]. To explore the biological functions of the two GPX4 alternative isoforms cGPX4 and iGPX4 in ferroptosis regulation under MAFLD condition, we employed the CRISPR/Cas9 system-based *Rosa26* insertion technology to generate two strains of mice, in which cGPX4 and iGPX4 were knocked in (herein referred as $R26^{cGPX4/cGPX4}$ mice and $R26^{iGPX4/iGPX4}$ mice). In $R26^{cGPX4/cGPX4}$ mice, we confirmed the genotype (Supporting Information Fig. S3A−S3D) and the knockin-mediate specific overexpression of cGPX4 isoform (Fig. S3E) in liver. $R26^{cGPX4/cGPX4}$ mice and age-matched wild-type mice ($R26^{WT/WT}$ mice) were fed normal chow or MCD for 4 weeks to establish MAFLD (Fig. 3A). MCD induced body weight loss in $R26^{WT/WT}$ mice and to a much lesser degree, in $R26^{cGPX4/cGPX4}$ mice (Fig. 3B). Knockin of cGPX4 isoform not only successfully inhibited elevated intracellular Fe^{2+} levels (Fig. 3C and Fig. S3F), but also suppressed protein expression of pro-ferroptosis factors including ACSL4, ALOX15, ferritin, transferrin, 3-nitrotyrosine, 4-HNE, TFR1 and ZIP14 (Fig. 3D and Fig. S3G). The $R26^{cGPX4/cGPX4}$ mice displayed reduced number of PI-positive dead cell number (Fig. 3E), decreased MDA (Fig. 3F), and increased GSH and SOD (Fig. 3G). Accordingly, liver injury upon MCD stress was blunted in $R26^{cGPX4/cGPX4}$ mice as opposed to $R26^{WT/WT}$ mice, as evidenced by alleviated serum ALT and AST levels (Fig. 3H), MAFLD activity score (Fig. 3I), macrophage infiltration ($F4/80^{+}$, Fig. 3J) and liver fibrosis (showed by Masson's trichrome staining [Fig. 3K] and Sirius Red staining [Fig. 3L]). The pro-inflammatory factors IL-1β and TNF-α were also attenuated in $R26^{cGPX4/cGPX4}$ mice in comparison with those in $R26^{WT/WT}$ mice (Fig. S3H). These results are in line with consensus that GPX4 inhibits ferroptosis, highlighting the protective action of cGPX4 in MAFLD.

3.4. *Isoform iGPX4 fuels ferroptosis in MAFLD model*

Next, we examined the functional role of iGPX4 in MAFLD mouse model. Isoform iGPX4 was successfully knocked into mice ($R26^{iGPX4/iGPX4}$ mice, Supporting Information Fig. S4A−S4E). The $R26^{iGPX4/iGPX4}$ and aged-matched $R26^{WT/WT}$ mice were challenged with MCD for 4 weeks (Fig. 4A). Upon MCD challenge, the decrease of body and liver weight (Fig. S4F) was comparable between $R26^{iGPX4/iGPX4}$ and $R26^{WT/WT}$ mice. MCD treatment evoked an elevation of Fe^{2+} content in $R26^{WT/WT}$ mouse liver and, to a greater extent, in $R26^{iGPX4/iGPX4}$ mice (Fig. 4B and Fig. S4G). MCD-induced increases of MDA and depletion of GSH, SOD in liver tissue was more pronounced in $R26^{iGPX4/iGPX4}$ mice (Fig. 4C). In line with these data, the increased lipid peroxidation markers 3-nitrotyrosine and 4-HNE were more pronounced in $R26^{iGPX4/iGPX4}$ mice compared with $R26^{WT/WT}$ mice in both chow and MCD conditions (Fig. 4D). Dihydroethidium fluorescence assay demonstrated a higher ROS level in liver tissue of $R26^{iGPX4/iGPX4}$ mice (Fig. 4E). PI staining demonstrated that the cell death in $R26^{iGPX4/iGPX4}$ mice liver was more pronounced than that in $R26^{WT/WT}$ mice (Fig. 4F). Numerous pro-ferroptosis factor, including ACSL4, ALOX15, ferritin, transferrin, TFR1 and ZIP14, were upregulated in $R26^{WT/WT}$ mice upon MCD and, to a much greater extent in $R26^{iGPX4/iGPX4}$ mice (Fig. 4G). $R26^{iGPX4/iGPX4}$ mice displayed higher expression of TNF-α and VCAM-1 in liver tissue (Fig. S4H). These results suggest that knockin of iGPX4 isoform does not inhibit, but rather promotes ferroptosis in MAFLD mouse model.

3.5. *Isoform iGPX4 aggravates glutathione/glutamine depletion, liver fibrosis and inflammation in MAFLD model*

We further investigated if the hyperactive ferroptosis in $R26^{iGPX4/iGPX4}$ mice would result in a more serious liver damage. Using immunofluorescence and immunohistochemistry TUNEL assays, $R26^{iGPX4/iGPX4}$ mice were found to exhibit more evident DNA fragmentation (Fig. 5A and B). Histological analyses demonstrated the MAFLD activity score (Fig. 5C) and macrophage infiltration (Fig. 5D) were worsened in $R26^{iGPX4/iGPX4}$ mice compared with $R26^{WT/WT}$ mice. Masson's trichrome staining, α-smooth muscle actin (α-SMA) immunohistochemistry staining and Sirius Red staining showed that MCD-induced liver fibrosis was accelerated in $R26^{iGPX4/iGPX4}$ mice (Fig. 5E). Similar results were observed in serum ALT and AST levels (Fig. 5F). To provide more information on the aggravated liver damage in $R26^{iGPX4/iGPX4}$ mice relative to $R26^{WT/WT}$ mice upon MCD, an RNA-sequencing analysis was applied to compare the gene change profile in liver between them. We found the altered genes include those controlling glutathione and glutamine metabolism (*e.g.*, *Gstt3*, *Gstm4*, *Gsta1*, *Gsta2*, *Gsr*, *Gstp1*, *Gsta4*, *Gclc*, *Pagr1a*, *Nags*, *Hmgcs1*, *Cyp4a12a* and *Cyp51*, Fig. 5G), cell survival/proliferation (*e.g.*, *Foxq1*, *Stat1*, *Hspd1 and Nsdhl*, Fig. 5H), liver fibrosis (*Timp1*, *Col1a1* and *Col1a2*, Fig. 5I) and pro-inflammation (*Nlrc3*, *Cx3cr1*, *Cxcr6* and *Tnfr-sf4*, Fig. 5J). These data support the more pronounced MCD-induced liver glutathione depletion, and steatohepatitis or liver damage in $R26^{iGPX4/iGPX4}$ mice than in $R26^{WT/WT}$ mice.

To confirm the role of iGPX4 in another MAFLD mouse model, $R26^{iGPX4/iGPX4}$ and $R26^{WT/WT}$ mice were treated with HFFD for 16 weeks. Lipid peroxidation markers 3-nitrotyrosine, 4-HNE and ALOX15 in $R26^{iGPX4/iGPX4}$ mice liver were significantly higher than that in $R26^{WT/WT}$ mice (Supporting Information Fig. S5A). Similar result was observed in MDA level (Fig. S5B) and ROS production (Fig. S5C). $R26^{iGPX4/iGPX4}$ mice had more serious liver damage, evidenced by the results of serum ALT and AST activities (Fig. S5D), MAFLD activity score (Fig. S5E) and liver fibrosis (Fig. S5F). Thus, we conclude that ferroptosis is fueled by the iGPX4 isoform, which further aggravates liver damage in MAFLD condition.

3.6. *Isoforms of cGPX4 and iGPX4 display opposing effects on ROS production and ferroptosis in hepatocytes*

To consolidate the detrimental role of iGPX4 isoform on liver injury, iGPX4 isoform was delivered in AML12 mouse

hepatocytes exposed to MCDM. The plasmids carrying cGPX4 and iGPX4 isoforms were transfected into AML12 cells, and forced-expression of cGPX4 and iGPX4 was confirmed by immunoblotting (Fig. 6A). We used Calcein-AM probe, a fluorescein-derived dye with green fluorescence that is quenched upon binding to ferrous ion (Fe^{2+}), to monitor the intracellular labile iron pool (LIP)[34]. The AML12 cells cultured with MCDM showed a remarkable reduction in fluorescence, suggesting an increased LIP (Fig. 6B). Overexpression of cGPX4 partially restored, whereas overexpression of iGPX4 decreased the Calcein-

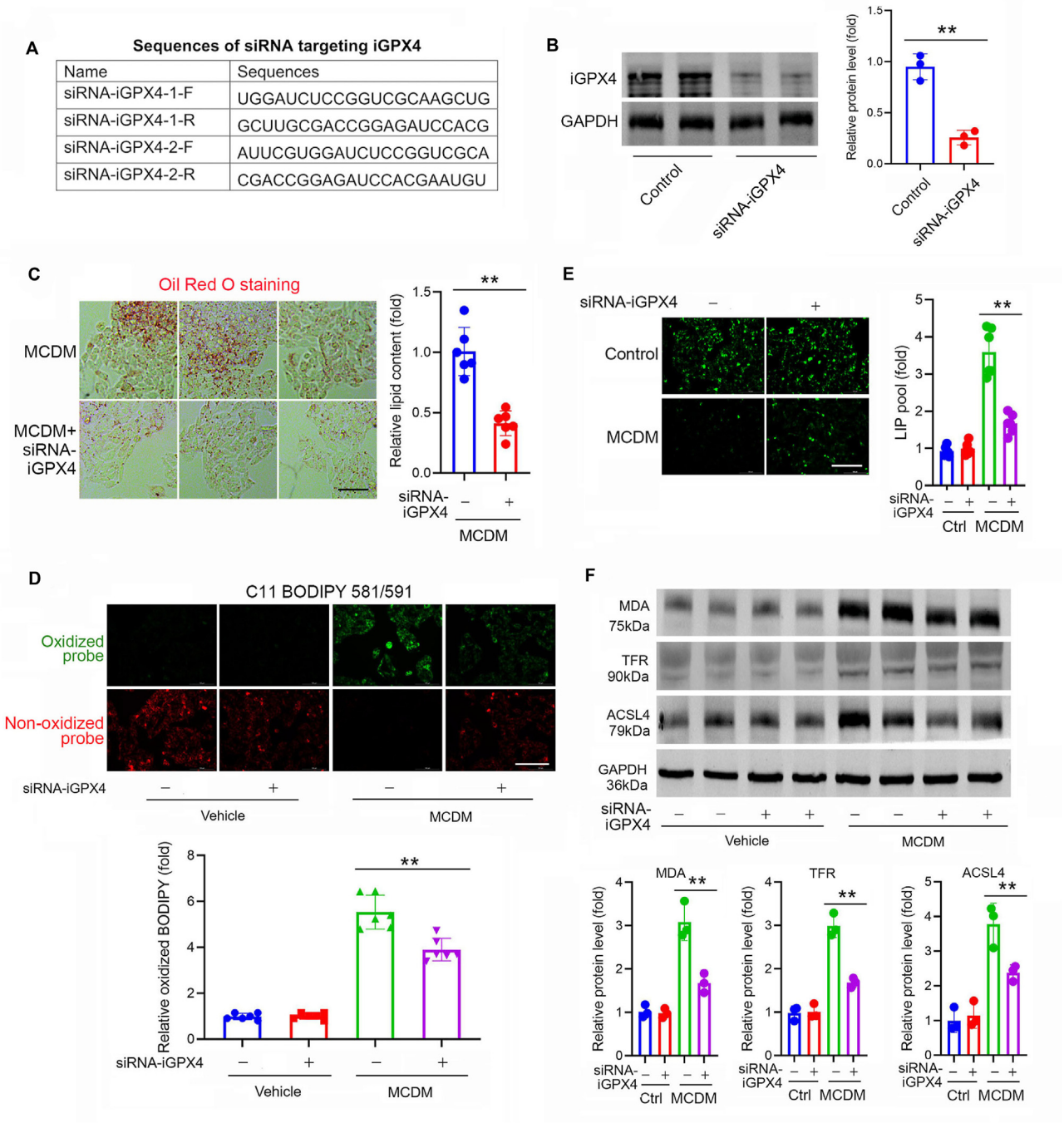

Figure 7 Knockdown of iGPX4 isoform alleviates ferroptosis and lipid oxidation in an *in vitro* MAFLD model. (A) Oligonucleotide sequence of siRNAs targeting to iGPX4. (B) Efficiency of knockdown of iGPX4 by siRNA was confirmed by immunoblotting. GAPDH was used as a loading control ($n = 3$ per group). (C) Oil Red O staining showing the lipid content (red) induced by MCDM was largely prevented by knocking down of iGPX4 with siRNA ($n = 6$ per group). Scale bar, 100 μm. (D) Staining of with C11 BODIPY 581/591 probe showing the lipid oxidation (green) induced by MCDM was largely attenuated by knocking down of iGPX4 with siRNA ($n = 6$ per group). Scale bar, 100 μm. (E) Staining of with Calcein-AM probe, a fluorescein-derived dye with green fluorescence that is quenched upon binding to ferrous ion (Fe^{2+}) showing the intracellular labile iron pool (LIP) induced by MCDM was prevented by knocking down of iGPX4 with siRNA ($n = 6$ per group). Scale bar, 100 μm. (F) Immunoblotting showing the levels of MDA, TFR and ACSL4 induced by MCDM were attenuated by knocking down of iGPX4 with siRNA ($n = 3$ per group). Data are presented as mean ± SEM, one way-ANOVA was performed; $^{**}P < 0.01$ *vs*. MCDM.

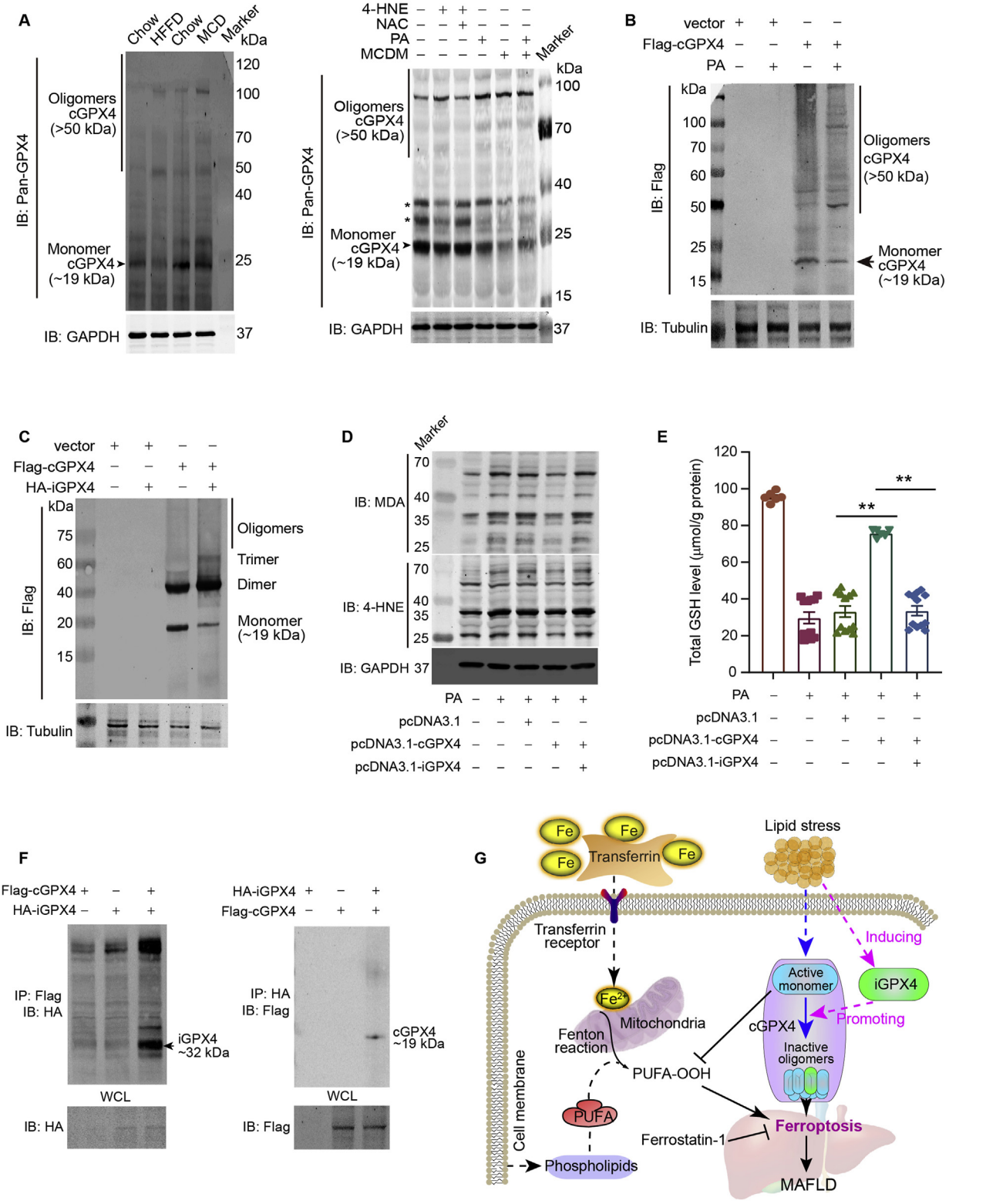

Figure 8 Isoform iGPX4 interacts with cGPX4 and promotes cGPX4 oligomerization to facilitate ferroptosis upon lipid stress. (A) Immunoblotting analysis with an anti-Pan-GPX4 antibody showing GPX4 oligomerization by comparing the cGPX4 monomer (~19 kDa) and oligomers (>50 kDa) in the liver tissues of mice fed normal chow diet, HFFD and MCD diet (left panel), as well as in AML12 hepatocytes stimulated under lipid stress by 4-HNE (20 μmol/L), PA (0.3 mmol/L) and MCDM (right panel). *N*-Acetyl-L-cysteine (NAC) was added into the culture medium to block the effect of 4-HNE. For detecting the GPX4 oligomerization, sample were incubated at 30 °C with EGS (300 μmol/L, 15 min) and lyzed with RIPA buffer with 5 mol/L guanidine-HCl. (B) Flag-tagged cGPX4 was transfected into AML12 hepatocyte cell line and the cells were stimulated with PA to evaluate the influence of lipid stress on cGPX4 oligomerization. The cGPX4 was detected with an antibody against Flag. The band in ~19 kDa (monomer cGPX4) was designated with an arrow. pcDNA3.1 was used as a vector. (C) Flag-tagged cGPX4

AM fluorescence, indicating that cGPX4 and iGPX4 protects and exacerbates, respectively, MCDM-induced iron overload (Fig. 6B). Flow cytometer analysis on Calcein-AM fluorescence intensity confirmed these results (Fig. 6C). In support of these, flow cytometry analysis with DCFH-DA, a ROS fluorescent probe, demonstrated that ROS production was inhibited by cGPX4 overexpression although it was enhanced by iGPX4 overexpression (Fig. 6D). The mitochondrial ROS content was quantified by observing the double fluorescence labeling with DCFH-DA and Mito-Tracker Red-CMXRos dyes. We found the mitochondrial ROS was induced in MCD-treated hepatocytes, which was attenuated by cGPX4 overexpression, but it was exacerbated by iGPX4 overexpression (Fig. 6E). The MDA production and loss in GSH upon MCDM challenge were inhibited by cGPX4 but not iGPX4 overexpression (Fig. 6F). Immunoblotting analysis demonstrated that the MCDM-induced ferroptosis markers including 3-nitrotyrosine, 4-HNE, ACSL4, ALOX15 and transferrin, were inhibited by cGPX4 overexpression (Fig. 6G) but deteriorated by iGPX4 overexpression (Fig. 6H). Notably, administration of ferrostatin-1 (Fer-1), a ferroptosis inhibitor, blocked the detrimental effects of iGPX4 on GSH activity and MDA, favoring the notion that iGPX4 exerts its action in a lipid peroxidation-dependent manner (Fig. 6I). The roles of cGPX4 and iGPX4 isoforms were also compared in PA-induced MAFLD cell model. The cGPX4 isoform reduced while iGPX4 isoform enhanced LIP (Supporting Information Fig. S6A). Moreover, cGPX4 isoform suppressed, whereas iGPX4 isoform elevated MDA level (Fig. S6B). All these results indicated that cGPX4 and iGPX4 exert opposite effects on ferroptosis in hepatocytes.

3.7. Knockdown of iGPX4 alleviates ROS, ferroptosis and cell injury

We also used pooled two siRNAs (Fig. 7A) to further confirm the detrimental action of iGPX4. These siRNAs successfully down-regulated iGPX4 (Fig. 7B). MCDM was used to induce lipid stress in cultured HepG2 cells. We found knockdown of iGPX4 significantly attenuated lipid content (Fig. 7C) and lipid oxidation (Fig. 7D). Moreover, knockdown of iGPX4 reduced intracellular liable iron pool (Fig. 7E). Finally, knockdown of iGPX4 alleviated ferroptosis, evidenced by the decreased protein of MDA, TFR and ACSL4 (Fig. 7F). These findings indicate that knockdown of iGPX4 alleviates ROS, ferroptosis and cell injury.

3.8. Isoform iGPX4 interacts with cGPX4 and promotes cGPX4 oligomerization to facilitate ferroptosis upon lipid stress

Excess oxidative stress leads to GPX4 linear oligomerization, yielding dead-end intermediates and oxidative inactivation of the enzyme[35]. To learn how the two isoforms function separately, we determined the cGPX4 monomer and oligomers in MAFLD mice liver using the antibody specific for cGPX4 rather than iGPX4. In the liver tissues of HFFD- or MCD-treated mice, the cGPX4 monomer (∼19 kDa) was reduced while the cGPX4 oligomers (>50 kDa) were significantly enhanced (Fig. 8A, left). In cultured AML12 hepatocytes, supplement of 4-HNE increased cGPX4 oligomers level, suggesting a direct oligomerization-promoting action of lipid-hydroperoxides. This effect was partially prevented by a well-established anti-oxidative agent *N*-acetyl-L-cysteine (NAC, Fig. 8A, right).

To better illustrate the cGPX4 oligomerization, we transfected AML12 hepatocytes with Flag-tagged cGPX4 and detected cGPX4 with an antibody against Flag. Upon PA stress, the band observed in ∼19 kDa site (cGPX4 monomer) was decreased while the high-molecular weight bands (cGPX4 oligomers) were increased (Fig. 8B). When the AML12 cells were transfected with Flag-tagged cGPX4 and HA-tagged iGPX4, we found that forced-overexpression of iGPX4 induced cGPX4 oligomerization (Fig. 8C). Immunoblotting analysis showed that the MDA and 4-HNE levels in cells co-overexpressed of cGPX4 and iGPX4 were higher than those in cells overexpressed cGPX4 alone upon PA stress (Fig. 8D). In agreement with this, cGPX4 of overexpression increased the GSH levels upon PA stimulation, whereas iGPX4 overexpression remarkably impaired this action (Fig. 8E). Notably, in AML12 cells overexpressed with Flag-tagged cGPX4 and HA-tagged iGPX4 simultaneously, co-immunoprecipitation analysis showed a direct interaction between cGPX4 and iGPX4 (Fig. 8F). The iGPX4−cGPX4 interaction was further confirmed using co-immunoprecipitation and nanoscale liquid chromatography coupled to tandem mass spectrometry (nano LC−MS/MS analysis (Supporting Information Fig. S7A). Plasmids carrying Flag-cGPX4 and HA-iGPX4 were co-transfected into PA-treated AML12 cells and the lysed cell extracts were immunoprecipitated with an antibody against HA-tag. After SDS-PAGE, the gel at the cGPX4 site was cut for MS. Five peptides were detected (Fig. S7B and S7C). Four peptides were within cGPX4 and iGPX4 (Fig. S7D−S7F), while one peptide was only within cGPX4 (Fig. S7G). These results strongly support the interaction between iGPX4 and cGPX4.

4. Discussion

Here, findings from our study provided compelling experimental evidence for the coordinated modulation of ferroptosis by the GPX4 canonical isoform (cGPX4) and inducible isoform (iGPX4) in the pathogenesis of MAFLD (Fig. 8G). *In vivo* and *in vitro* studies showed that knockin or overexpression of iGPX4 isoform does not inhibit, but rather promotes ferroptosis and MAFLD.

and HA-tagged iGPX4 were transfected into AML12 hepatocyte cell line to evaluate the influence of iGPX4 on cGPX4 oligomerization. The cGPX4 was detected with an antibody against Flag. The band in ∼19 kDa (monomer cGPX4) was designated with an arrow. (D) Immunoblotting analysis showing overexpression of iGPX4 (pcDNA3.1-iGPX4) antagonized the cGPX4 overexpression (pcDNA3.1-cGPX4)-induced decrease of MDA and 4-HNE protein adducts in AML12 hepatocytes under PA stimuli (0.3 mmol/L). (E) Overexpression of iGPX4 abolished the cGPX4 overexpression-induced restoration of GSH activity in AML12 hepatocytes under PA stimuli (0.3 mmol/L). Data are presented as mean ± SEM and analyzed by one-way ANOVA followed by Tukey's *post hoc* test; $^{**}P < 0.01$. (F) Flag-tagged cGPX4 and HA-tagged iGPX4 were co-transfected into AML12 hepatocyte cell line to evaluate the interaction between iGPX4 and cGPX4 with co-immunoprecipitation. WCL, whole cell lysate. Heavy chain and light chain were labeled. (G) A working model for the functional regulation of GPX4 alternative isoforms in ferroptosis control and hepatic damage in MAFLD. Lipid stress induces iGPX4, which interacts with cGPX4 and facilitates the transformation of cGPX4 from monomer (active) to oligomers (inactive). The isoform iGPX4 promotes ferroptosis and deteriorate MFALD.

This detrimental role of iGPX4 seems to be in contrary to the conventional view that GPX4 should be a key safeguard against lipid stress-induced ferroptosis, which was also confirmed by our results using cGPX4-knockin mice. Mechanistically, we found that iGPX4 isoform promoted cGPX4 oligomerization through incorporating itself into enzymatic-inactive high-molecular-weight GPX4 oligomers. Finally, co-immunoprecipitation and mass spectrum analyses confirmed the interaction between iGPX4 and cGPX4. By revealing a detrimental role of iGPX4 in ferroptosis-related disease that is in contrary to cGPX4, our findings may add important knowledge to the ferroptosis signaling transduction and regulation.

We provided evidence for the first time on the unconventional role of nGPX4 as an inducible GPX4 isoform (iGPX4) upon lipotoxicity stress in addition to its known nuclear GPX4 isoform in sperm. More importantly, the function of this isoform in the face of hepatic lipid stress seems to be different from its conventional function in sperm. Our experimental results in cultured hepatocytes demonstrated a redistribution of iGPX4 isoform from nucleus to cytoplasm upon lipid stress. Notably, we also found that cGPX4 was not restricted to mitochondria. Given that membrane-derived extra-mitochondrial lipid peroxidation drives ferroptosis[6,36], the precise location where GPX4 exerts its anti-ferroptotic action remains an open question. Moreover, all these *in vitro* results suggest that iGPX4 may not only regulate sperm maturation in testis as a nuclear selenocysteine enzyme, but also contribute to the pathophysiology associated with lipotoxicity and ferroptosis in liver as a cytosol effector. To this end, *in vivo* study with $R26^{iGPX4/iGPX4}$ mice was performed. To our surprise, the $R26^{iGPX4/iGPX4}$ mice displayed an aggravated ferroptosis, as well as the enhanced steatohepatitis, fibrosis and liver damage in both HFFD- and MCD-induced MAFLD animal models. Our RNA-sequencing analysis noted a disrupted metabolism on glutathione and glutamate in $R26^{iGPX4/iGPX4}$ mice upon MCD stimuli, supporting the notion that defective glutamine fueling and glutathione generation reprogramming are pivotal events in progression of MAFLD[37]. The altered profile of glutathione and glutamate metabolism in liver tissues from $R26^{iGPX4/iGPX4}$ mice also confirmed involvement of ferroptosis signaling in these mice in comparison with the WT mice in the face of MCD challenge.

In accordance with the detrimental role of iGPX4 in MAFLD development *in vivo*, overexpression of iGPX4 in hepatocytes sustained the PA- or MCDM-induced ferroptosis. A rational explanation is that iGPX4 isoform functions as a negative regulator for cGPX4 in liver, the most important organ of GSH synthesis[4]. This speculation was supported by the finding in the present study that overexpression of iGPX4 directly downregulated cGPX4 monomer level and enhanced cGPX4 oligomerization. Generally speaking, downregulation of GPX4 has long been considered as a prominent biomarker or biological cue driving ferroptosis in human diseases such as ischemia[38], renal failure[6], tumor[39,40] and stroke[41], yet few has explained the precise nature behind downregulated GPX4 protein. GPX4 level in intestines was reported to be reduced by ~90% within 15 min upon ischemia/reperfusion stress[38]. Such quick decline of active GPX4 (~19 kDa) protein level strongly suggests that there might be a rapid degradation of GPX4 protein. In our hands, the canonical GPX4 protein (~19 kDa), often deemed as the typical 'GPX4', was indeed downregulated in liver tissue from MAFLD patients and two different MAFLD mouse models. GPX4 possesses biological activity as a monomer and forms enzymatic-inactive oligomerization or polymerization upon excess oxidative stress[35]. We noted that the oligomerization of cGPX4 was substantially driven by lipid peroxidation *in vivo* and *in vitro*, while overexpression of iGPX4 isoform further promoted this phenomenon. These suggest that the iGPX4 isoform is not a partner acting in concert with cGPX4 but conversely acts as an antagonist in MAFLD condition. From a biological perspective, this makes sense as iGPX4 isoform is quiescent and always kept at low transcriptional level under normal condition but induced upon specific stress and finally modulates cGPX4 status. According to our results, we speculate that iGPX4 mRNA may be regulated by lipid stress at post-transcriptional level, which needs further study.

Of note, we found only with the lysis buffer containing potent chaotropic agents such as guanidine-HCl, the inactive high-molecular cGPX4 oligomers can be detected using Western blotting, while chaotropic agents are not commonly used for tissue lysis. Thus, we consider the transformation of GPX4 from monomer to oligomers may be neglected in previous works[42]. The total protein was considered to be dissolved in the supernatant during lysis process. GPX4 oligomers was undissolved and thus undetectable if chaotropic agents (such as guanidine-HCl) was not added. So, if researchers did not use chaotropic agents during lysis process, the high-molecular-weight GPX4 oligomers/polymers were discarded, and the total GPX4 protein level cannot be accurate. As chaotropic agents were not commonly used in Western blotting, loss of GPX4 observed under various stimuli may not completely reflect the authentic change of pan GPX4 protein. Taking together, we postulate that iGPX4 promotes the transformation of cGPX4 from monomer to oligomer, which decreases monomer cGPX4 level (~19 kDa) and ultimately leads to cGPX4 inactivation.

Our results may have limitations. MCD diet is not a physiological relevant diet for MAFLD. However, MCD diet is a classical method of inducing NASH[43], which is the most rapidly growing etiology for liver failure and indication for liver transplantation worldwide. An MCD diet better mimicked the pathological findings of severe human NASH than did other dietary models. Inflammation, fibrosis and hepatocyte apoptosis in mice fed a MCD diet developed much more quickly and severely than those fed an HFD or Western diets[43]. However, the MCD model has limitation due to that the mice fed an MCD diet always show significant weight loss, low serum insulin, fasting glucose and did not display insulin resistance. These disparities with the metabolic profile of human NASH are uncontroversial flaws of MCD model. Consequently, MCD is suitable study of cell death, inflammation and fibrosis but not lipid/glucose hemostasis and insulin resistance. Generally, two distinct MAFLD models should be conducted to confirm the phenotypes. In the present work, we also performed experiments in a HFFD-induced MAFLD model. This model mimics the metabolic dysfunction, steatosis and Inflammation in MAFLD very well[31,44–46]. All the biological function of iGPX4 were confirmed in these two animal models, further validating the detrimental role of iGPX4 in MAFLD process. As ferroptosis is only critical for MAFLD, but also highly involved in acetaminophen-induced acute liver injury[47], alcoholic liver disease[48], hepatic ischemia–reperfusion injury in liver transplantation[49] and liver fibrosis[50], our findings on GPX4 isoforms switch in ferroptosis regulation would open a new perspective for potential to manipulate ferroptosis as a therapeutic strategy in liver disorders.

5. Conclusions

In summary, data presented in this study reveal for the first time that an iGPX4 isoform contributes to ferroptosis modulation and hepatic damage through antagonizing the function of cGPX4 in MAFLD. These findings suggest that targeting iGPX4 isoform may be a promising strategy for MAFLD treatment.

Acknowledgments

This work was supported by the grants from National Natural Science Foundation of China (82073915, 91849135, 81673485, 81773719, 81973312 and 81971306), National Key Research and Development Project (2018YFA0108301, China), Shanghai Science and Technology Commission Experimental Animal Grants (21XD1424900, 19140904700, 19140904900 and 21S11901200, China), Shanghai Shuguang Program (19SG32, China), Shanghai "Rising Stars of Medical Talent" Youth Development Program-Youth Medical Talents-Clinical Pharmacist Program [SHWRS(2020)_087, China]. We thank the patients and their families. We would like to thank Cyagen Biosciences for their work in generation of knockin mice. We also wish to acknowledge the Majorbio BioTech (Shanghai, China) for technical support in liver tissue RNA-sequencing.

Author contributions

Pei Wang and Fuming Shen conceived and designed research; Jie Tong, Dongjie Li, Hongbo Meng, Diyang Sun, Xiuting Lan, Min Ni, Jiawei Ma, Feiyan Zeng, Sijia Sun, Jiangtao Fu, Guoqiang Li, Qingxin Ji, Guoyan Zhang, Qirui Shen, Yuanyuan Wang, Jiahui Zhu, Yi Zhao, Xujie Wang, Yi Liu and Shenxi Ouyang performed experiments; Chunquan Sheng provided material; Jie Tong, Dongjie Li, Fuming Shen and Pei Wang analyzed data; Fuming Shen and Pei Wang wrote the manuscript; All authors contributed with productive discussions and knowledge to the final version of this manuscript.

Conflicts of interest

All authors declare no conflicts of interest.

Appendix A. Supporting information

Supporting data to this article can be found online at https://doi.org/10.1016/j.apsb.2022.02.003.

References

1. Tilg H, Effenberger M. From NAFLD to MAFLD: when pathophysiology succeeds. *Nat Rev Gastroenterol Hepatol* 2020;**17**:387−8.
2. Eslam M, Newsome PN, Sarin SK, Anstee QM, Targher G, Romero-Gomez M, et al. A new definition for metabolic dysfunction-associated fatty liver disease: an international expert consensus statement. *J Hepatol* 2020;**73**:202−9.
3. Yan T, Yan N, Wang P, Xia Y, Hao H, Wang G, et al. Herbal drug discovery for the treatment of nonalcoholic fatty liver disease. *Acta Pharm Sin B* 2020;**10**:3−18.
4. Dixon SJ, Lemberg KM, Lamprecht MR, Skouta R, Zaitsev EM, Gleason CE, et al. Ferroptosis: an iron-dependent form of non-apoptotic cell death. *Cell* 2012;**149**:1060−72.
5. Yang WS, SriRamaratnam R, Welsch ME, Shimada K, Skouta R, Viswanathan VS, et al. Regulation of ferroptotic cancer cell death by GPX4. *Cell* 2014;**156**:317−31.
6. Friedmann Angeli JP, Schneider M, Proneth B, Tyurina YY, Tyurin VA, Hammond VJ, et al. Inactivation of the ferroptosis regulator Gpx 4 triggers acute renal failure in mice. *Nat Cell Biol* 2014;**16**:1180−91.
7. Galluzzi L, Vitale I, Aaronson SA, Abrams JM, Adam D, Agostinis P, et al. Molecular mechanisms of cell death: recommendations of the nomenclature committee on cell death 2018. *Cell Death Differ* 2018;**25**:486−541.
8. Ingold I, Berndt C, Schmitt S, Doll S, Poschmann G, Buday K, et al. Selenium utilization by GPX4 is required to prevent hydroperoxide-induced ferroptosis. *Cell* 2018;**172**:409−422.e21.
9. Zou Y, Palte MJ, Deik AA, Li H, Eaton JK, Wang W, et al. A GPX4-dependent cancer cell state underlies the clear-cell morphology and confers sensitivity to ferroptosis. *Nat Commun* 2019;**10**:1617.
10. Doll S, Proneth B, Tyurina YY, Panzilius E, Kobayashi S, Ingold I, et al. ACSL4 dictates ferroptosis sensitivity by shaping cellular lipid composition. *Nat Chem Biol* 2017;**13**:91−8.
11. Wenzel SE, Tyurina YY, Zhao J, St Croix CM, Dar HH, Mao G, et al. PEBP1 wardens ferroptosis by enabling lipoxygenase generation of lipid death signals. *Cell* 2017;**171**:628−641.e26.
12. Chu B, Kon N, Chen D, Li T, Liu T, Jiang L, et al. ALOX12 is required for p53-mediated tumour suppression through a distinct ferroptosis pathway. *Nat Cell Biol* 2019;**21**:579−91.
13. Bersuker K, Hendricks JM, Li Z, Magtanong L, Ford B, Tang PH, et al. The CoQ oxidoreductase FSP1 acts parallel to GPX4 to inhibit ferroptosis. *Nature* 2019;**575**:688−92.
14. Doll S, Freitas FP, Shah R, Aldrovandi M, da Silva MC, Ingold I, et al. FSP1 is a glutathione-independent ferroptosis suppressor. *Nature* 2019;**575**:693−8.
15. Protchenko O, Baratz E, Jadhav S, Li F, Shakoury-Elizeh M, Gavrilova O, et al. Iron chaperone poly rC binding protein 1 protects mouse liver from lipid peroxidation and steatosis. *Hepatology* 2021;**73**:1176−93.
16. Feng H, Schorpp K, Jin J, Yozwiak CE, Hoffstrom BG, Decker AM, et al. Transferrin receptor is a specific ferroptosis marker. *Cell Rep* 2020;**30**:3411−34123.e7.
17. Yu Y, Jiang L, Wang H, Shen Z, Cheng Q, Zhang P, et al. Hepatic transferrin plays a role in systemic iron homeostasis and liver ferroptosis. *Blood* 2020;**136**:726−39.
18. Mao C, Liu X, Zhang Y, Lei G, Yan Y, Lee H, et al. DHODH-mediated ferroptosis defence is a targetable vulnerability in cancer. *Nature* 2021;**593**:586−90.
19. Pfeifer H, Conrad M, Roethlein D, Kyriakopoulos A, Brielmeier M, Bornkamm GW, et al. Identification of a specific sperm nuclei selenoenzyme necessary for protamine thiol cross-linking during sperm maturation. *FASEB J* 2001;**15**:1236−8.
20. Wang H, An P, Xie E, Wu Q, Fang X, Gao H, et al. Characterization of ferroptosis in murine models of hemochromatosis. *Hepatology* 2017;**66**:449−65.
21. Sun X, Ou Z, Chen R, Niu X, Chen D, Kang R, et al. Activation of the p62−Keap1−NRF2 pathway protects against ferroptosis in hepatocellular carcinoma cells. *Hepatology* 2016;**63**:173−84.
22. Gao R, Kalathur RKR, Coto-Llerena M, Ercan C, Buechel D, Shuang S, et al. YAP/TAZ and ATF4 drive resistance to sorafenib in hepatocellular carcinoma by preventing ferroptosis. *EMBO Mol Med* 2021;**13**:e14351.
23. Du J, Wan Z, Wang C, Lu F, Wei M, Wang D, et al. Designer exosomes for targeted and efficient ferroptosis induction in cancer *via* chemo-photodynamic therapy. *Theranostics* 2021;**11**:8185−96.
24. Xu Q, Zhan G, Zhang Z, Yong T, Yang X, Gan L. Manganese porphyrin-based metal-organic framework for synergistic sonodynamic therapy and ferroptosis in hypoxic tumors. *Theranostics* 2021;**11**:1937−52.

25. Tang H, Li C, Zhang Y, Zheng H, Cheng Y, Zhu J, et al. Targeted manganese doped silica nano GSH-cleaner for treatment of liver cancer by destroying the intracellular redox homeostasis. *Theranostics* 2020;**10**:9865−87.
26. Zhang Z, Guo M, Shen M, Kong D, Zhang F, Shao J, et al. The BRD7−P53−SLC25A28 axis regulates ferroptosis in hepatic stellate cells. *Redox Biol* 2020;**36**:101619.
27. Shen M, Li Y, Wang Y, Shao J, Zhang F, Yin G, et al. N^6-Methyladenosine modification regulates ferroptosis through autophagy signaling pathway in hepatic stellate cells. *Redox Biol* 2021;**47**:102151.
28. Sorrentino P, D'Angelo S, Ferbo U, Micheli P, Bracigliano A, Vecchione R. Liver iron excess in patients with hepatocellular carcinoma developed on non-alcoholic steato-hepatitis. *J Hepatol* 2009;**50**:351−7.
29. Qi J, Kim JW, Zhou Z, Lim CW, Kim B. Ferroptosis affects the progression of nonalcoholic steatohepatitis *via* the modulation of lipid peroxidation-mediated cell death in mice. *Am J Pathol* 2020;**190**:68−81.
30. Li X, Wang TX, Huang X, Li Y, Sun T, Zang S, et al. Targeting ferroptosis alleviates methionine-choline deficient (MCD)-diet induced NASH by suppressing liver lipotoxicity. *Liver Int* 2020;**40**:1378−94.
31. Liu D, Zhang P, Zhou J, Liao R, Che Y, Gao MM, et al. TNFAIP3 interacting protein 3 overexpression suppresses nonalcoholic steatohepatitis by blocking TAK1 activation. *Cell Metab* 2020;**31**:726−740 e8.
32. Santhekadur PK, Kumar DP, Sanyal AJ. Preclinical models of non-alcoholic fatty liver disease. *J Hepatol* 2018;**68**:230−7.
33. Wang ET, Sandberg R, Luo S, Khrebtukova I, Zhang L, Mayr C, et al. Alternative isoform regulation in human tissue transcriptomes. *Nature* 2008;**456**:470−6.
34. Yang WS, Kim KJ, Gaschler MM, Patel M, Shchepinov MS, Stockwell BR. Peroxidation of polyunsaturated fatty acids by lipoxygenases drives ferroptosis. *Proc Natl Acad Sci U S A* 2016;**113**:E4966−75.
35. Scheerer P, Borchert A, Krauss N, Wessner H, Gerth C, Hohne W, et al. Structural basis for catalytic activity and enzyme polymerization of phospholipid hydroperoxide glutathione peroxidase-4 (GPx4). *Biochemistry* 2007;**46**:9041−9.
36. Kong N, Chen X, Feng J, Duan T, Liu S, Sun X, et al. Baicalin induces ferroptosis in bladder cancer cells by downregulating FTH1. *Acta Pharm Sin B* 2021;**11**:4045−54.
37. Simon J, Nunez-Garcia M, Fernandez-Tussy P, Barbier-Torres L, Fernandez-Ramos D, Gomez-Santos B, et al. Targeting hepatic glutaminase 1 ameliorates non-alcoholic steatohepatitis by restoring very-low-density lipoprotein triglyceride assembly. *Cell Metab* 2020;**31**:605−622 e10.
38. Li Y, Feng D, Wang Z, Zhao Y, Sun R, Tian D, et al. Ischemia-induced ACSL4 activation contributes to ferroptosis-mediated tissue injury in intestinal ischemia/reperfusion. *Cell Death Differ* 2019;**26**:2284−99.
39. Liu Y, Song Z, Liu Y, Ma X, Wang W, Ke Y, et al. Identification of ferroptosis as a novel mechanism for antitumor activity of natural product derivative a2 in gastric cancer. *Acta Pharm Sin B* 2021;**11**:1513−25.
40. Liang Y, Zhang L, Peng C, Zhang S, Chen S, Qian X, et al. Tumor microenvironments self-activated nanoscale metal-organic frameworks for ferroptosis based cancer chemo-dynamic/photothermal/chemo therapy. *Acta Pharm Sin B* 2021;**11**:3231−43.
41. Alim I, Caulfield JT, Chen Y, Swarup V, Geschwind DH, Ivanova E, et al. Selenium drives a transcriptional adaptive program to block ferroptosis and treat stroke. *Cell* 2019;**177**:1262−1279 e25.
42. Toppo S, Vanin S, Bosello V, Tosatto SC. Evolutionary and structural insights into the multifaceted glutathione peroxidase (Gpx) superfamily. *Antioxid Redox Signal* 2008;**10**:1501−14.
43. Lau JK, Zhang X, Yu J. Animal models of non-alcoholic fatty liver disease: current perspectives and recent advances. *J Pathol* 2017;**241**:36−44.
44. Wang S, Tao J, Chen H, Kandadi MR, Sun M, Xu H, et al. Ablation of Akt2 and AMPKalpha2 rescues high fat diet-induced obesity and hepatic steatosis through Parkin-mediated mitophagy. *Acta Pharm Sin B* 2021;**11**:3508−26.
45. Li DJ, Sun SJ, Fu JT, Ouyang SX, Zhao QJ, Su L, et al. NAD^+-boosting therapy alleviates nonalcoholic fatty liver disease *via* stimulating a novel exerkine Fndc5/irisin. *Theranostics* 2021;**11**:4381−402.
46. Hua X, Sun DY, Zhang WJ, Fu JT, Tong J, Sun SJ, et al. P7C3-A20 alleviates fatty liver by shaping gut microbiota and inducing FGF21/FGF1, *via* the AMP-activated protein kinase/CREB regulated transcription coactivator 2 pathway. *Br J Pharmacol* 2021;**178**:2111−30.
47. Yamada N, Karasawa T, Kimura H, Watanabe S, Komada T, Kamata R, et al. Ferroptosis driven by radical oxidation of *n*-6 polyunsaturated fatty acids mediates acetaminophen-induced acute liver failure. *Cell Death Dis* 2020;**11**:144.
48. Zhou Z, Ye TJ, DeCaro E, Buehler B, Stahl Z, Bonavita G, et al. Intestinal SIRT1 deficiency protects mice from ethanol-induced liver injury by mitigating ferroptosis. *Am J Pathol* 2020;**190**:82−92.
49. Yamada N, Karasawa T, Wakiya T, Sadatomo A, Ito H, Kamata R, et al. Iron overload as a risk factor for hepatic ischemia−reperfusion injury in liver transplantation: potential role of ferroptosis. *Am J Transplant* 2020;**20**:1606−18.
50. Kong Z, Liu R, Cheng Y. Artesunate alleviates liver fibrosis by regulating ferroptosis signaling pathway. *Biomed Pharmacother* 2019;**109**:2043−53.